Research Article | Vol. 30, No. 13 / 20 Jun 2022 / Optics Express 22661
Optics EXPRESS

Anisotropic third-harmonic generation of exfoliated As_2S_3 thin flakes

RAVI P. N. TRIPATHI,[1] XIAODONG YANG,[1,3] AND JIE GAO[1,2,4]

[1]Department of Mechanical and Aerospace Engineering, Missouri University of Science and Technology, Rolla, Missouri 65409, USA
[2]Department of Mechanical Engineering, Stony Brook University, Stony Brook, New York 11794, USA
[3]yangxia@mst.edu
[4]jie.gao.5@stonybrook.edu

Abstract: Van der Waals (vdW) materials have recently attracted significant interest in the context of orientation-dependent linear and nonlinear optical properties. Recently, arsenic trisulfide (As_2S_3) or orpiment is identified as a new vdW layered material having anisotropic vibrational and optomechanical responses due to the reduced in-plane crystal symmetry, but its nonlinear optical response is still not well understood yet. Herein, the anisotropic third-harmonic generation (THG) response of mechanically exfoliated As_2S_3 thin flakes is reported. The polarization-dependent evolution of THG emission from butterfly-shaped pattern to four-lobe pattern is comprehensively explored. Moreover, the third-order nonlinear susceptibility of As_2S_3 crystal is extracted by analyzing the thickness-dependent THG emission. We anticipate that the discussed results will not only update the existing understanding on the nonlinear light-matter interaction in anisotropic vdW materials, but also promote future applications in integrated photonic circuits, on-chip nonlinear signal processing, and polarization-sensitive optical devices.

1. Introduction

Van der Waals (vdW) materials with strong light-matter interaction, broadband and tunable optical absorption, and high nonlinear conversion efficiency, have facilitated a versatile testbed for miniaturized nonlinear photonic devices such as ultrafast optical modulators, wavelength-dependent multiplexers, ultrafast photonic circuits, and mode-locked/Q-switched lasers [1–5]. A variety of vdW materials including graphene [6], vdW heterostructures [7–10], and transition metal dichalcogenides (TMDs) [11] have been explored in the context of nonlinear optical signal generation, four-wave mixing, nonlinear refraction and saturable absorption. For instance, TMDs are explored for second-harmonic generation (SHG) and four-wave mixing, while graphene nanosheets are utilized for optically or electrically driven third-harmonic generation (THG) and terahertz nonlinearity [6,12,13]. Recently, the intrinsic structural anisotropy in vdW layered materials is envisioned as an additional degree of freedom to manipulate and modulate the nonlinear optical responses, which leads to the exploration of a novel class of anisotropic layered materials such as black phosphorous (BP), ReS_2, GeSe, GeAs, SiP, and $SnSe_2$ [14–19]. Moreover, there has been a recent trend in vdW materials research about the exploration of new layered materials, in order to further expand the horizon of the adaptability and versatility for utilizing these materials in the relevant applications. Following this trend, As_2S_3 (orpiment) is recently introduced into the vdW material family [20]. The optical properties of the As_2S_3 crystal are relatively well understood in the context of infrared material transmittivity [21], photoconductivity [22], and tunability of optical bandgap [23], which make this material attractive for photonic applications. Recently, mechanically exfoliated As_2S_3 membranes have been explored to demonstrate anisotropic vibrational and optomechanical properties and the estimated Young's modulus [20]. It is worth noting that anisotropic nonlinear optical response of layered As_2S_3 crystal is still unexplored so far.

#457858 https://doi.org/10.1364/OE.457858
Journal © 2022 Received 7 Mar 2022; revised 30 May 2022; accepted 31 May 2022; published 7 Jun 2022

Optics EXPRESS

Motivated with this, herein we demonstrate anisotropic THG emission in mechanically exfoliated As_2S_3 thin flakes. The exfoliated flakes are investigated using optical microscope and atomic force microscope (AFM) to estimate the flake shape, size, thickness, and surface smoothness. Furthermore, polarization-resolved Raman spectroscopy technique is used to identify the crystal axis of the probed flakes. Then, the THG emission response with respect to the input linear polarization is investigated in the prepared As_2S_3 flakes, where the polarization-dependent evolution of THG emission from butterfly-shaped pattern to four-lobe pattern is studied. Moreover, the third-order nonlinear susceptibility of As_2S_3 crystal is estimated via the recorded thickness-dependent THG emission power. We envision that our findings will be relevant in advancing future applications in integrated photonic circuits, on-chip nonlinear signal processing, as well as promoting compact photonic and optoelectronic devices such as nonlinear beam converters, photodetectors, and optical switches.

2. Preparation and characterization of mechanically exfoliated As_2S_3 flakes

Arsenic trisulfide occurs as orpiment mineral in nature, consisting of arsenic (As) and sulfur (S). It has a monoclinic crystal structure belonging to $P2_1/n$ space group, which consists of 20 atoms in a unit cell [24] with the lattice parameters of $a = 11.46$ Å, $b = 9.57$ Å, $c = 4.22$ Å, and $\beta = 90.5°$ [25]. The schematic illustration of the atomic arrangement in a typical As_2S_3 crystal from three side views is depicted in Fig. 1(a). The structure is made of the corrugated layers of heart-shaped six-membered rings of the corner sharing As_2S_3 pyramids. The individual layers are regarded as a macromolecular layer of As_2S_3 composition stacked via weak vdW dipole-induced nondirectional intermolecular forces [26], which makes mechanical exfoliation feasible from the bulk crystal. Figure 1(b) shows the picture of a bulk As_2S_3 crystal (2D Semiconductors), which is used to attain thin flakes with different thicknesses ranging from 8 nm to 52 nm via mechanical exfoliation process using Nitto tape (SPV 224) and scotch tape. The exfoliated flakes are then transferred onto the cleaned glass substrates. Figures 1(c) and 1(d) show the AFM images of 8

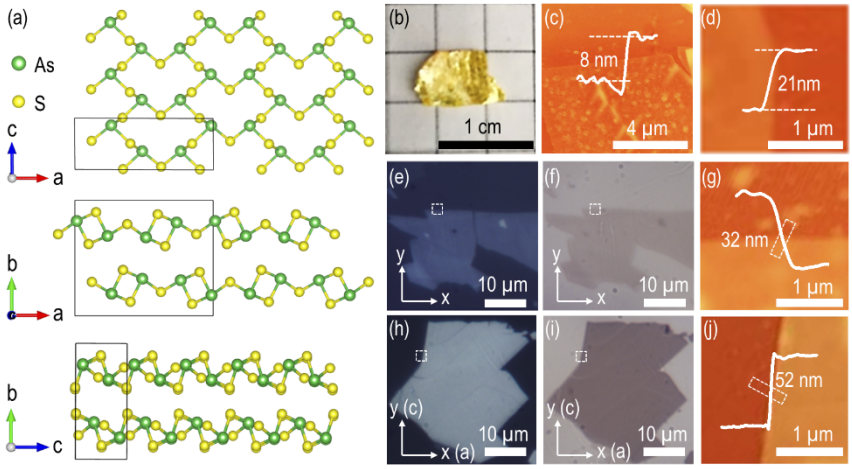

Fig. 1. Sample preparation and microscopic characterization. (a) Schematic illustration of As_2S_3 crystal structure viewed along the *b*-axis, *c*-axis, and *a*-axis. (b) Picture of bulk As_2S_3 crystal. (c), (d) AFM images of 8 nm and 21 nm-thick mechanically exfoliated As_2S_3 flakes. (e), (h) and (f), (i) Optical microscope images in reflection and transmission mode of 32 nm and 52 nm flakes. The white boxes in optical images indicate the AFM scanned regions. (g), (j) Captured AFM images of 32 nm and 52 nm flakes, where the AFM line profiles signify the flake thickness and surface smoothness.

Optics EXPRESS

nm and 21 nm thick As_2S_3 flakes. Also, the optical microscope images of 32 nm and 52 nm thick As_2S_3 flakes in reflection and transmission mode are shown in Figs. 1(e), 1(f) and 1(h), 1(I). The corresponding captured AFM images are shown in Figs. 1(g) and 1(j), which signify the flake thickness and surface smoothness.

3. Anisotropic Raman scattering and identification of crystal axis

Next, the prepared flakes are characterized using polarization-resolved Raman spectroscopy technique to get an insight on intrinsic structural anisotropy of the probed crystal and determination of the crystal's axes [16–18,27,28], which will be further used to investigate the anisotropic nonlinear THG emission in As_2S_3 crystals. Figure 2(a) shows the collected Raman spectrum from the 52 nm-thick As_2S_3 flake at the linear polarization angle of 150° with respect to the x-axis of the probed flake using a 632.8 nm He-Ne laser excitation source. The He-Ne laser beam is focused using a 40× objective lens (NA = 0.65) to illuminate the flake and the back reflected light is collected with the same objective lens. The signal is then filtered by an edge filter (Semrock, LP02-633RE-25) and routed to a spectrometer (Horiba, iHR 550) for recording the Raman scattering spectrum. The recorded Raman spectrum exhibits several distinct Raman peaks in the range of 75–400 cm^{-1}, located at 134, 157, 181, 205, 252, 289, 311, 329, and 355 cm^{-1}. It is noted that the majority of the identified Raman modes shows an excellent match with the previously reported Raman spectrum for As_2S_3 crystal [20]. Subsequently, we investigate the polarization dependence of Raman intensity under parallel polarization configuration, where a linear polarizer analyzer in the collection path is set in the parallel direction with respect to the input linear polarization in order to resolve the parallel component of the Raman signal. Figure 2(b) shows the color map of polarization-resolved Raman spectra for the 52 nm-thick As_2S_3 crystal. To get further insight on the anisotropic evolution of different Raman modes, the measured angular plots of individual Raman modes are corroborated with the theoretical model. For As_2S_3 crystal belonging to the monoclinic crystal family with $P2_1/n$ space group, the corresponding Raman tensors for A_g and B_g Raman modes can be expressed as [27]

$$R(A_g) = \begin{bmatrix} ae^{i\emptyset_a} & 0 & de^{i\emptyset_d} \\ 0 & be^{i\emptyset_b} & 0 \\ de^{i\emptyset_d} & 0 & ce^{i\emptyset_c} \end{bmatrix} \tag{1}$$

$$R(B_g) = \begin{bmatrix} 0 & ee^{i\emptyset_e} & 0 \\ ee^{i\emptyset_e} & 0 & f\ e^{i\emptyset_f} \\ 0 & fe^{i\emptyset_f} & 0 \end{bmatrix} \tag{2}$$

where a, b, c, d, e, and f are the amplitudes of Raman tensor elements, and $\emptyset_a$, $\emptyset_b$, $\emptyset_c$, $\emptyset_d$, $\emptyset_e$, and $\emptyset_f$ indicate the corresponding phases. Considering the polarization states of incident and scattering beams, the resultant expressions of the parallel polarization components for Raman A_g and B_g modes are

$$I_{A_g}^{//} \propto \left[(|a|\ sin^2\theta + |b|\ cos\emptyset_{ba} cos^2\theta)^2 + (|b|\ sin\emptyset_{ba} cos^2\theta)^2\right] \tag{3}$$

$$I_{B_g}^{//} \propto |e|^2\ sin^2 2\theta \tag{4}$$

where $\emptyset_{ba} = \emptyset_b - \emptyset_a$ shows the phase difference between a and b components of Raman tensor. Figures 2(c)–2(h) show the angular plots for different Raman modes. The measured values are indicated with black squares, whereas the theoretical fittings are shown with brown solid lines. It

Optics EXPRESS

is observed that the identified Raman modes are anisotropic in nature, which endorse the presence of the reduced in-plane structural symmetry in the probed crystal. The recorded A_g modes exhibit four-lobe patterns with two unequal Raman intensity maxima along two perpendicular directions. The Raman modes at 134, 181 and 311 cm^{-1} show the primary maxima along 0° and 180°, whereas the Raman modes at 205 and 355 cm^{-1} give the primary maxima residing along around 90° and 270°. In contrast to Raman A_g modes, the recorded B_g mode at 289 cm^{-1} shows the typical four-lobe pattern of equal maxima along 45°, 135°, 225° and 315°. In addition, the retrieved relative magnitudes of Raman tensor elements $|a|$, $|b|$, and $|e|$ for different A_g and B_g modes are listed in Table 1. It is clear that $|a|$ is larger than $|b|$ for the A_g modes at 134, 181 and 311 cm^{-1}, while $|a|$ is smaller than $|b|$ for the A_g modes at 205 and 355 cm^{-1}. Based on the previous literatures [7–10,16–18,27–29], anisotropic Raman A_g modes are used to identify the crystal's axes. Hence, 0° and 90° directions are labelled as the *a*-axis and *c*-axis of the probed flake, which are further used in performing the polarization-dependent anisotropic THG study.

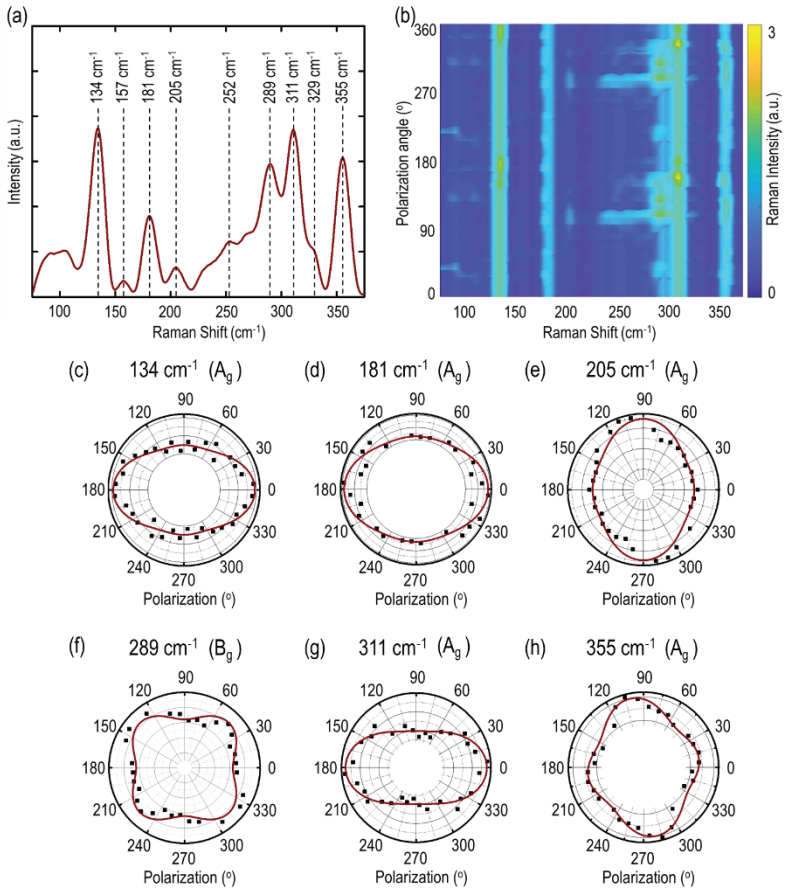

Fig. 2. Anisotropic Raman scattering and determination of crystal axis. (a) Collected Raman spectrum from the 52-nm thick As_2S_3 flake with the identified Raman modes indicated with black dashed lines. (b) Color map of the recorded polarization-resolved Raman spectra in parallel polarization configuration. (c)–(h) Angular plots of Raman intensity variations for Raman modes at 134, 181, 205, 289, 311, and 355 cm^{-1}. The measured values are indicated with black squares, whereas the theoretical fittings are shown with brown solid lines.

Optics EXPRESS

Table 1. The retrieved relative magnitudes of Raman tensor elements of A_g and B_g modes

	A_g mode					B_g mode
Raman shift	134 cm^{-1}	181 cm^{-1}	205 cm^{-1}	311 cm^{-1}	355 cm^{-1}	289 cm^{-1}
$\|a\|$	1.4	1.08	0.49	1.38	1.06	–
$\|b\|$	1.13	0.93	0.85	0.99	1.21	–
$\|e\|$	–	–	–	–	–	0.7

4. Anisotropic THG and determination of third-order nonlinear susceptibility

The anisotropic THG emission in As_2S_3 crystal is investigated using a 1560 nm pulse laser source (pulse width 90 fs, repetition rate 80 MHz), with the 1.5 μm beam spot size and the average pump power of 1.17 mW, which is equivalent to the 9.20 GW/cm^2 peak irradiance. The incident laser beam is focused on the flake using a 40× objective lens (NA = 0.65). The transmitted THG emission from the flake is collected using a 100× objective lens (NA = 0.7) from the other side of the glass substrate. A shortpass filter is engaged in the collection path to reject the laser contribution, then the filtered signal is routed to a spectrometer (Horiba, iHR 550) for recording the THG spectrum.

Figure 3(a) shows the collected THG emission spectrum from the 52 nm-thick As_2S_3 flake, showing the peak intensity at 520 nm which is exactly one third of the pump wavelength at 1560 nm. To further ensure the THG emission process, the emission power is recorded as a function of input pump power and fitted with a cubic power law, as shown in the double-scale log plot of Fig. 3(b). The measured power values are indicated with black squares, while the cubic power fit is shown with brown solid line. The retrieved slope of 2.92 ± 0.08 ensures the THG emission process. Next, the in-plane anisotropic THG emission is probed in As_2S_3 flakes by collecting the THG intensity as a function of the input linear polarization angle of the pump beam. The input linear polarization is controlled by introducing a linear polarizer and a half-wave plate in the excitation path, while the recorded THG intensity components of $I_x^{(3\omega)}$ and $I_y^{(3\omega)}$ are further resolved in the direction along two crystal's axes of the a-axis ($\theta = 0°$) and c-axis ($\theta = 90°$), respectively, by engaging a linear polarizer analyzer in the collection path along each axis. The identification of the crystal's axes is performed for all the flakes using the polarization-resolved Raman spectroscopy measurements in accordance with the Raman A_g modes. Figures 3(c)–3(h) display the recorded angular plots of THG emission for several exfoliated As_2S_3 flakes with the thicknesses of 13, 21, 32, 44, 52, and 102 nm. It can be observed that the measured THG emission is highly anisotropic in nature for all the flakes. However, the resultant total THG emission resembles as a butterfly-shaped pattern for the flakes of 13, 21, 32, and 52 nm, which is substantially different from the four-lobe pattern for the flakes of 44 and 102 nm. It is inferred that the anisotropic nature of THG emission is consistent in all the investigated As_2S_3 flakes, but the resultant total THG emission varies from butterfly-shape pattern to four-lobe pattern. The measured values along the x-axis (a-axis) and y-axis (c-axis), and the total values are represented with red squares, blue dots, and upper black triangles, respectively. Noticeably, the shape of THG emission pattern is highly sensitive to the values of nonlinear susceptibility $\chi^{(3)}$ tensor elements. In addition, the contribution of the off-axis tensor elements also plays a crucial role in determining the shape of THG emission pattern. In case of the butterfly-shaped THG emission pattern, the contribution of the off-axis tensor elements is relatively high. Nevertheless, such contribution continuously varies from flake to flake, as shown in the THG emission measurements. It is worthwhile noting that the butterfly-shaped THG emission pattern exhibits variation as per the investigated flake. Hence, the mechanical exfoliation process can also be regarded as one of the key factors. Moreover, since the flake preparation involves several rounds of exfoliation, there is the significant probability of introducing the exfoliation led deformation in the crystal, so that

Optics EXPRESS

the contribution of the off-axis tensor elements may vary significantly for different flakes. Such phenomena have been observed in several previous studies, where the observed dissimilarities between the values of the $\chi^{(3)}$ tensor elements in the two scenarios of emission pattern are attributed to the mechanical exfoliation induced deformation in the crystal [30–32].

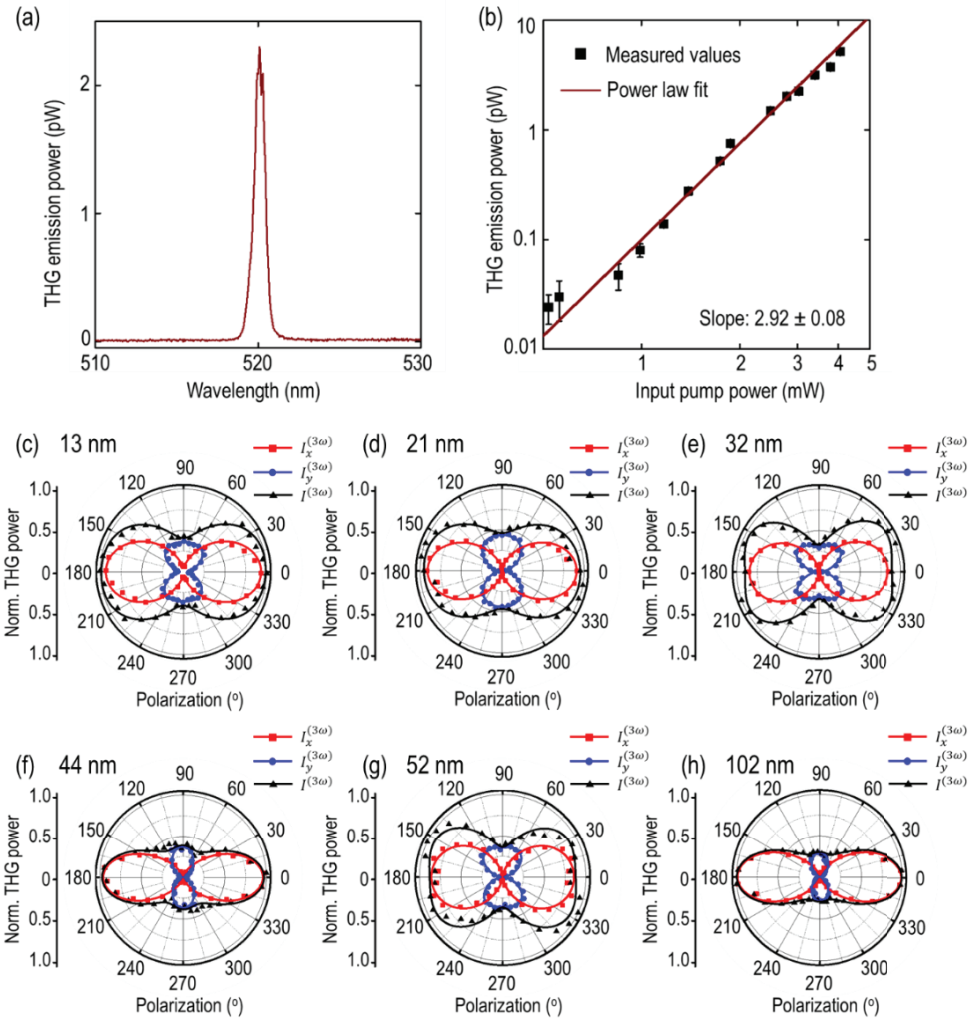

Fig. 3. Polarization-dependent anisotropic THG emission. (a) Recorded THG spectrum from the 52 nm-thick As_2S_3 flake. (b) Double log-scale plot of THG emission power as a function of input pump power. Measured values are indicated with black squares, while the linear fit is shown with brown solid line. (c)–(h) Collected angular plots of THG emission from several As_2S_3 flakes with the thicknesses of 13, 21, 32, 44, 52, and 102 nm. Measured values along x-axis ($I_x^{(3\omega)}$) and y-axis ($I_y^{(3\omega)}$) and total values ($I^{(3\omega)}$) are denoted with red squares, blue dots, and black upper triangles. The corresponding theoretical fits using the nonlinear susceptibility model is shown with solid lines in their respective colors.

To get further insight about the observed THG emission patterns, the measured values are corroborated with a theoretical model of the third-order nonlinear susceptibility. Since As_2S_3 crystal belongs to monoclinic crystal family, the third-order nonlinear susceptibility in the

Optics EXPRESS

contracted form can be expressed as [27,28]

$$\chi^{(3)} = \begin{bmatrix} \chi_{11} & 0 & \chi_{13} & 0 & \chi_{15} & \chi_{16} & \chi_{17} & \chi_{18} & 0 & 0 \\ 0 & \chi_{22} & 0 & \chi_{24} & 0 & 0 & 0 & 0 & \chi_{29} & \chi_{20} \\ \chi_{31} & 0 & \chi_{33} & 0 & \chi_{35} & \chi_{36} & \chi_{37} & \chi_{38} & 0 & 0 \end{bmatrix} \quad (5)$$

where the first subscript of 1, 2, and 3 denotes x, y, and z respectively, and the second subscript refers to the combination of three components as

xxx	yyy	zzz	yzz	yyz	xzz	xxz	xyy	xxy	xyz
1	2	3	4	5	6	7	8	9	0

Taking into account the incident pump beam with frequency ω and linear polarization angle θ with respect to the a-axis (x-axis) of the crystal, the linearly polarized pump beam can be expressed as $\vec{E}^{(\omega)} = \hat{x}(|E_0|cos\theta) + \hat{y}(|E_0|sin\theta)$. In accordance with the experimental configuration, the incident beam resides in the x-y plane, thus the z-containing tensor elements are neglected and only four nonzero terms of χ_{11}, χ_{18}, χ_{22} and χ_{29} contribute to the in-plane THG emission. The resultant expression for THG emission along the x-axis and y-axis can be written as

$$I_x^{(3\omega)} \propto (\chi_{11}\, cos^3\theta + 3\chi_{18}\, cos\theta\, sin^2\theta)^2 \quad (6)$$

$$I_y^{(3\omega)} \propto (\chi_{22}\, sin^3\theta + 3\chi_{29}\, sin\theta\, cos^2\theta)^2 \quad (7)$$

Equations (6) and (7) are used to fit the measured THG emission patterns and the theoretical fits are shown in Figs. 3(c)–3(h) with solid lines in the corresponding colors. It is clear that the theoretical fits give a good agreement with the experimental data. It is worth noting that the x-component THG emission $I_x^{(3\omega)}$ remains a dipolar two-lobe pattern for all the flakes, whereas the y-component $I_y^{(3\omega)}$ exhibits the change from a conventional two-lobe pattern to a four-lobe pattern, leading to the variation in the resultant total THG emission $I^{(3\omega)}$ from a four-lobe pattern into a butterfly-shaped pattern. This interesting feature can be explained in terms of the relative contributions of nonlinear susceptibility tensor elements. Figure 4(a) shows the plot of the extracted average relative magnitudes of $\chi^{(3)}$ elements as a function of the flake thickness, which underlines the significant variations in the relative magnitudes of $\chi^{(3)}$ elements. Based on the extracted $\chi^{(3)}$ values, it is inferred that the relative contributions of the off-axis tensor elements χ_{18} and χ_{29} compared to the on-axis elements χ_{11} and χ_{22} play a crucial role in determining the shape of total THG emission pattern. According to the expression for $I_x^{(3\omega)}$ in Eq. (6), since the value of χ_{11} is much higher compared to χ_{18} for all the flakes, no significant off-axis contribution is involved in determining the THG emission pattern of $I_x^{(3\omega)}$, which results in a dipolar two-lobe pattern. In contrast, the difference between the values of χ_{22} and χ_{29} is not large enough for the flakes of 13, 21, 32 and 52 nm, hence the contribution of the off-axis tensor element χ_{29} will be significant, which leads to the four-lobe pattern signature for the THG emission $I_y^{(3\omega)}$. Consequently, the total THG emission pattern emerges as a butterfly-shaped pattern. On the other hand, for the 44 nm and 102 nm-thick flakes, the difference between χ_{22} and χ_{29} is high, which leads to a dipolar two-lobe pattern for the THG emission $I_y^{(3\omega)}$. Thereby, the resultant total THG emission pattern evolves as a typical four-lobe pattern. The distinct changes in the values of the off-axis tensor elements χ_{18} and χ_{29} in the two cases may arise from the crystal lattice deformation induced in the mechanical exfoliation process, which has also been observed in the exfoliated GeSe flakes [18]. Nevertheless, the average relative magnitudes of $\chi^{(3)}$ elements are extracted as $\chi_{11} : \chi_{18} : \chi_{22} : \chi_{29} = 1 : 0.29 : 0.60 : 0.29$, which also endorses the intrinsic

Optics EXPRESS

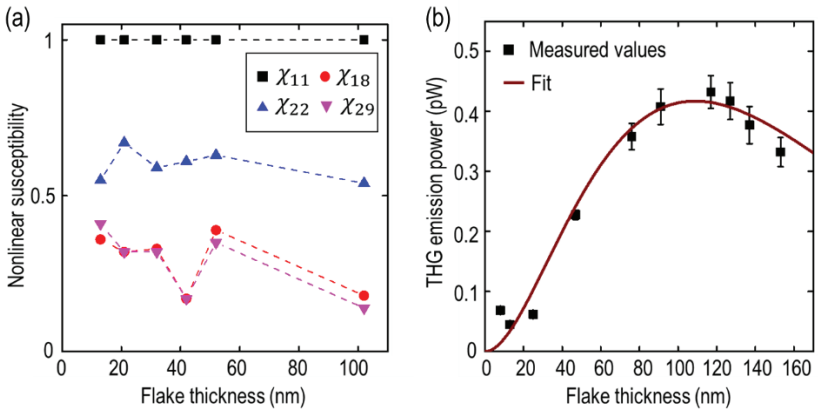

Fig. 4. Nonlinear optical susceptibility and thickness-dependent THG emission. (a) Retrieved relative magnitudes of nonlinear susceptibility tensor elements (χ_{11}, χ_{18}, χ_{22}, χ_{29}) as a function of the flake thickness. (b) Recorded THG emission power as a function of the flake thickness. Measured values are indicated with black squares with error bars, while the theoretical fitting is shown with brown solid line.

nonlinear optical anisotropy in As_2S_3 crystals. Furthermore, the average THG anisotropy ratio ($|\chi_{11}|^2/|\chi_{22}|^2$) is calculated as 2.78.

Finally, we estimate the third-order nonlinear susceptibility of As_2S_3 crystal via collecting the THG emission power as a function of the flake thickness. The thickness-dependent THG emission measurement is conducted while the incident linear polarization is along the x–axis. The total THG emission is collected as no analyzer is engaged in the collection path. Figure 4(b) shows the recorded THG emission power for As_2S_3 flakes with the thicknesses ranging from 8 to 152 nm. The THG emission power is recorded at the pump power of 1.17 mW (9.20 GW/cm^2 peak irradiance) with the 1.5 μm beam spot size. Noticeably, the THG emission power first exhibits an continuous increase up to 102 nm and afterwards an exponentially decay for larger thickness. This phenomenon of thickness-dependent THG emission can be explained in the context of two simultaneous competitive processes of optical gain and loss. For flake thicknesses lower than 102 nm, the THG emission is proportional to the square of the flake thickness. It is worth noting that the absorption loss is not strong at low flake thickness, so there is a systematic increase in THG emission power up to 102 nm. In contrast, at higher thicknesses, the presence of strong optical absorption plays a crucial role in attenuating the THG signal propagation through the flakes. Consequently, the exponential decay of THG signal is observed for the flake thickness larger than 102 nm. Importantly, the exponential decay trend offers an opportunity to extract the imaginary part of the refractive index (k_3) at λ_3 = 520 nm for As_2S_3 crystal, by fitting the THG emission power with the expression $P^{(3\omega)}(l) = Al^2\exp\left(-\frac{4\pi k_3 l}{\lambda_3}\right)$, where A is a constant, l is the flake thickness. The retrieved value of k_3 is found to be 0.76. In addition, the third-order nonlinear susceptibility of As_2S_3 crystal can be further extracted by the following expression [29],

$$\left|\chi^{(3)}\right|^2 = \left[\frac{16\sqrt{n_3^2+k_3^2}\,n_1^3\epsilon_0^2c^4f_{rep}^2W^4\tau^2\left[\frac{\pi}{4\ln 2}\right]^3P^{(3\omega)}}{9\omega^2l^2P^{(\omega)^3}}\left(\frac{\left(\frac{4\pi^2k_3^2l^2}{\lambda_3^2}+\Delta k^2l^2\right)}{e^{-\frac{4\pi k_3 l}{\lambda_3}}-2\cos(\Delta kl)\,e^{-\frac{2\pi k_3 l}{\lambda_3}}+1}\right)e^{\frac{4\pi k_3 l}{\lambda_3}}\right] \tag{8}$$

by considering other experimental parameters related to the laser excitation source and the As_2S_3 crystal, including repetition rate f_{rep} = 80 MHz, beam spot size W = 1.5 μm, pulse width

Optics EXPRESS

$\tau = 90$ fs, and the refractive indices of the As_2S_3 crystal at the fundamental wavelength n_1 and the THG wavelength n_3. Based on the previous literature [33], the refractive index values of As_2S_3 are considered as $n_1 = 2.44$ and $n_3 = 2.73$. $\Delta k = \frac{6\pi}{\lambda_1}(n_1 - n_3)$ represents the phase mismatch between the pump beam and the forward propagating THG beam in transmission configuration. Thus, the $\chi^{(3)}$ value of As_2S_3 crystal can be estimated as 1.20×10^{-20} m^2/V^2, which has the similar order of magnitude as other recently explored vdW materials [16–18,27–29]. Moreover, since the estimated $\chi^{(3)}$ value of As_2S_3 crystal from Eq. (8) is based on the measured THG emission power under the incident linear polarization along the x–axis, it represents the χ_{11} element. According to the average relative magnitudes of $\chi^{(3)}$ elements, the actual estimated values of the four independent coefficients of χ_{11}, χ_{18}, χ_{22} and χ_{29} are 1.20×10^{-20}, 0.348×10^{-20}, 0.72×10^{-20}, and 0.348×10^{-20} m^2/V^2, respectively.

5. Conclusion

In summary, we have demonstrated the in-plane anisotropic THG emission from mechanically exfoliated As_2S_3 thin flakes. First, the crystal's axes of As_2S_3 flakes are determined by performing polarization-resolved Raman spectroscopy. The anisotropic nature of Raman scattering for different Raman modes are studied by corroborating the experimental observation with the theoretical expression of Raman intensity under parallel polarization configuration. It is shown that the anisotropic nature of As_2S_3 crystal is facilitated by the reduced in-plane crystal symmetry. Then, the anisotropic nature of THG emission is investigated, showing that the As_2S_3 crystal exhibits two different types of the resultant total THG emission patterns as four-lobe pattern and butterfly-shaped pattern. This unique feature is further explained in the context of the relative contributions of the off-axis nonlinear susceptibility tensor elements compared to the on-axis elements. Finally, the third-order nonlinear susceptibility of As_2S_3 crystal is extracted from the thickness-dependent THG emission. With this hindsight, we envisage that these findings will not only provide a comprehensive understanding of anisotropic nonlinear light-matter interactions in vdW materials especially in the context of the polarization-dependent evolution of THG emission patterns, but also further pave a way to the advancement in future applications in optical communication, secured data processing, integrated photonic circuits, and compact nonlinear optical devices.

Funding. National Science Foundation (DMR-1552871, ECCS-1653032).

Acknowledgments. The authors thank Eric Bohannan for the help in acquiring the AFM data.

Disclosures. The authors declare no conflicts of interest.

Data availability. Data underlying the results presented in this paper are not publicly available at this time but may be obtained from the authors upon reasonable request.

References

1. Y. Cheng, H. Hong, H. Zhao, C. Wu, Y. Pan, C. Liu, Y. Zuo, Z. Zhang, J. Xie, and J. Wang, "Ultrafast optical modulation of harmonic generation in two-dimensional materials," Nano Lett. **20**(11), 8053–8058 (2020).
2. T. Jiang, K. Yin, C. Wang, J. You, H. Ouyang, R. Miao, C. Zhang, K. Wei, H. Li, and H. Chen, "Ultrafast fiber lasers mode-locked by two-dimensional materials: review and prospect," Photonics Res. **8**(1), 78–90 (2020).
3. J. Wu, H. Ma, P. Yin, Y. Ge, Y. Zhang, L. Li, H. Zhang, and H. Lin, "Two-dimensional materials for integrated photonics: recent advances and future challenges," Small Sci. **1**(4), 2000053 (2021).
4. F. Xia, H. Wang, D. Xiao, M. Dubey, and A. Ramasubramaniam, "Two-dimensional material nanophotonics," Nat. Photonics **8**(12), 899–907 (2014).
5. J. W. You, S. R. Bongu, Q. Bao, and N. C. Panoiu, "Nonlinear optical properties and applications of 2D materials: theoretical and experimental aspects," Nanophotonics **8**(1), 63–97 (2018).
6. G. Soavi, G. Wang, H. Rostami, D. G. Purdie, D. De Fazio, T. Ma, B. Luo, J. Wang, A. K. Ott, and D. Yoon, "Broadband, electrically tunable third-harmonic generation in graphene," Nat. Nanotechnol. **13**(7), 583–588 (2018).
7. R. P. N. Tripathi, J. Gao, and X. Yang, "Naturally occurring layered mineral franckeite with anisotropic Raman scattering and third-harmonic generation responses," Sci. Rep. **11**(1), 8510 (2021).
8. A. Dasgupta, J. Gao, and X. Yang, "Naturally occurring 2D heterostructure nagyágite with anisotropic optical properties," Adv. Mater. Interfaces **8**(23), 2101106 (2021).

Optics EXPRESS

9. A. Dasgupta, X. Yang, and J. Gao, "Naturally occurring van der Waals heterostructure lengenbachite with strong in-plane structural and optical anisotropy," npj 2D Mater. Appl. **5**(1), 88 (2021).
10. A. Dasgupta, J. Gao, and X. Yang, "Natural van der Waals heterostructure cylindrite with highly anisotropic optical responses," npj 2D Mater. Appl. **5**(1), 74 (2021).
11. X. Wen, Z. Gong, and D. Li, "Nonlinear optics of two-dimensional transition metal dichalcogenides," InfoMat **1**(3), 317–337 (2019).
12. A. Autere, H. Jussila, Y. Dai, Y. Wang, H. Lipsanen, and Z. Sun, "Nonlinear optics with 2D layered materials," Adv. Mater. **30**(24), 1705963 (2018).
13. S. Kovalev, H. A. Hafez, K.-J. Tielrooij, J.-C. Deinert, I. Ilyakov, N. Awari, D. Alcaraz, K. Soundarapandian, D. Saleta, and S. Germanskiy, "Electrical tunability of terahertz nonlinearity in graphene," Sci. Adv. **7**(15), eabf9809 (2021).
14. C. Wang, G. Zhang, S. Huang, Y. Xie, and H. Yan, "The optical properties and plasmonics of anisotropic 2D materials," Adv. Opt. Mater. **8**(5), 1900996 (2020).
15. L. Li, W. Han, L. Pi, P. Niu, J. Han, C. Wang, B. Su, H. Li, J. Xiong, Y. Bando, and T. Zhai, "Emerging in-plane anisotropic two-dimensional materials," InfoMat **1**(1), 54–73 (2019).
16. H. Sar, J. Gao, and X. Yang, "In-plane anisotropic third-harmonic generation from germanium arsenide thin flakes," Sci. Rep. **10**(1), 14282 (2020).
17. H. Sar, J. Gao, and X. Yang, "2D layered SiP as anisotropic nonlinear optical material," Sci. Rep. **11**(1), 6372 (2021).
18. A. Dasgupta, J. Gao, and X. Yang, "Anisotropic third-harmonic generation in layered germanium selenide," Laser Photonics Rev. **14**(6), 1900416 (2020).
19. Y. Abate, D. Akinwande, S. Gamage, H. Wang, M. Snure, N. Poudel, and S. B. Cronin, "Recent progress on stability and passivation of black phosphorus," Adv. Mater. **30**(29), 1704749 (2018).
20. M. Šiškins, M. Lee, F. Alijani, M. R. van Blankenstein, D. Davidovikj, H. S. J. van der Zant, and P. G. Steeneken, "Highly anisotropic mechanical and optical properties of 2D layered As_2S_3 membranes," ACS Nano **13**(9), 10845–10851 (2019).
21. R. Frerichs, "New optical glasses with good transparency in the infrared," J. Opt. Soc. Am. **43**(12), 1153–1157 (1953).
22. D. F. Blossey and R. Zallen, "Surface and bulk photoresponse of crystalline As_2S_3," Phys. Rev. B **9**(10), 4306–4313 (1974).
23. N. Miao, J. Zhou, B. Sa, B. Xu, and Z. Sun, "Few-layer arsenic trichalcogenides: emerging two-dimensional semiconductors with tunable indirect-direct band-gaps," J. Alloys Compd. **699**, 554–560 (2017).
24. L. Debbichi, H. Kim, T. Björkman, O. Eriksson, and S. Lebègue, "First-principles investigation of two-dimensional trichalcogenide and sesquichalcogenide monolayers," Phys. Rev. B **93**(24), 245307 (2016).
25. N. Morimoto, "The Crystal Structure of Orpiment (As_2S_3) Refined," Mineral. Mag. **1**(3), 160–169 (1954).
26. G. V. Gibbs, A. F. Wallace, R. Zallen, R. T. Downs, N. L. Ross, D. F. Cox, and K. M. Rosso, "Bond paths and van der Waals interactions in orpiment, As_2S_3," J. Phys. Chem. A **114**(23), 6550–6557 (2010).
27. R. P. N. Tripathi, X. Yang, and J. Gao, "Van der Waals layered mineral getchellite with anisotropic linear and nonlinear optical responses," Laser Photonics Rev. **15**(12), 2100182 (2021).
28. R. P. N. Tripathi, J. Gao, and X. Yang, "Anisotropic optical responses of layered thallium arsenic sulfosalt gillulyite," Sci. Rep. **11**(1), 22002 (2021).
29. N. Youngblood, R. Peng, A. Nemilentsau, T. Low, and M. Li, "Layer-tunable third-harmonic generation in multilayer black phosphorus," ACS Photonics **4**(1), 8–14 (2017).
30. M. J. L. F. Rodrigues, C. J. S. de Matos, Y. W. Ho, H. Peixoto, R. E. P. de Oliveira, H.-Y. Wu, A. H. C. Neto, and J. Viana-Gomes, "Resonantly increased optical frequency conversion in atomically thin black phosphorus," Adv. Mater. **28**(48), 10693–10700 (2016).
31. A. Autere, C. R. Ryder, A. Säynätjoki, L. Karvonen, B. Amirsolaimani, R. A. Norwood, N. Peyghambarian, K. Kieu, H. Lipsanen, M. C. Hersam, and Z. Sun, "Rapid and Large-Area Characterization of Exfoliated Black Phosphorus Using Third-Harmonic Generation Microscopy," J. Phys. Chem. Lett. **8**(7), 1343–1350 (2017).
32. Q. Cui, R. A. Muniz, J. E. Sipe, and H. Zhao, "Strong and anisotropic third-harmonic generation in monolayer and multilayer ReS_2," Phys. Rev. B **95**(16), 165406 (2017).
33. W. S. Rodney, I. H. Malitson, and T. A. King, "Refractive index of arsenic trisulfide," J. Opt. Soc. Am. **48**(9), 633–636 (1958).